An internally consistent framework for calculating cascading probabilistic earthquake risk and its application to a case study in New Zealand

Jose Moratalla*,David Burbidge, Jean Roger, Katie Jones, Angela Griffin, Christof Mueller, Uma Ashok, Finn Scheele, Yaseen Mahmood, Edith Bretherton

Earth Sciences New Zealand, Lower Hutt, New Zealand

**Correspondence to: moratalla.jmm@gmail.com*

Supplementary material

S1. Case Study Region

Napier City is situated on the east coast of New Zealand's North Island, within the Hawke's Bay region. The city occupies a predominantly flat coastal plain of approximately 106 km² and supports a population of 62,241 inhabitants (2018 Census, Stats NZ, accessed 12/04/2022). With a density of about 540 inhabitants per km², Napier represents a significant urban centre in the region. Its coastal morphology is defined by a 5 m-high gravel ridge extending north and south of Bluff Hill, uplifted abruptly during the 1931 Mw 7.8 Hawke's Bay earthquake (Komar, 2010). The city is further characterized by two major estuarine systems—the Ahuriri estuary and the confluence of the Ngaruroro, Tutaekuri, and Karamu rivers—which influence both its hydrological and sedimentary dynamics (Haidekker et al., 2016).

The largest earthquake to affect the region was the Mw 7.8 Hawke's Bay event of 3 February 1931, during which cascading hazards significantly contributed to the damage and disruption of the built environment. Napier City is particularly vulnerable to liquefaction, as shown by multiple studies (Fairless and Berrill, 1984; Dowrick, 1998; Dellow et al., 2003; Rosser and Dellow, 2017). The 1931 earthquake triggered widespread liquefaction, disrupting lifeline services and damaging residential properties.

Its location along the shoreline of the North Island´s east coast, right in front of the Hikurangi SZ located offshore, makes earthquake induced tsunami another key hazard to be considered. It is also possible that the area may be exposed to tsunamis generated by underwater landslides, similar to the rest of the eastern continental margin of New Zealand (Roger et al, 2024). However, consideration of the underwater landslide generated tsunami is beyond the scope of the paper, in part due to the considerable uncertainties that currently exist with the likelihood and size of this potential source of local tsunamis.

Figure S1 The coastal context of Napier city: (a), (b) and (c) Napier Port, with the storage areas hosting containers and timbers, as well as dangerous goods; (d) the entrance of the Ahuriri Estuary; (e) the Ahuriri Estuary at mid-tide; (f) East Pier Beach; (g) Ahuriri River and marina; (h) Napier Beach (East Coast); (i) Ravensdown Industrial Complex (Awatoto).

S2. Earthquake hazard modelling

Subduction zone geometry

The geometry of the Hikurangi subduction interface used in this study follows Williams et al. (2013), which refines the earlier Ansell and Bannister (1996) model. Williams et al. (2013) provide a detailed parametric surface representation of the HSZ interface, allowing depth and surface normal vectors to be determined at any point. The model integrates multiple datasets, including earthquake hypocentre locations and tomographic inversion results, Active-source seismic reflection and refraction data, and the bathymetric expression of the trench.

The resulting interface geometry (Figure S1) defines the sources for earthquake and tsunami generation and was converted into .xml format compatible with OpenQuake (GEM, 2019).

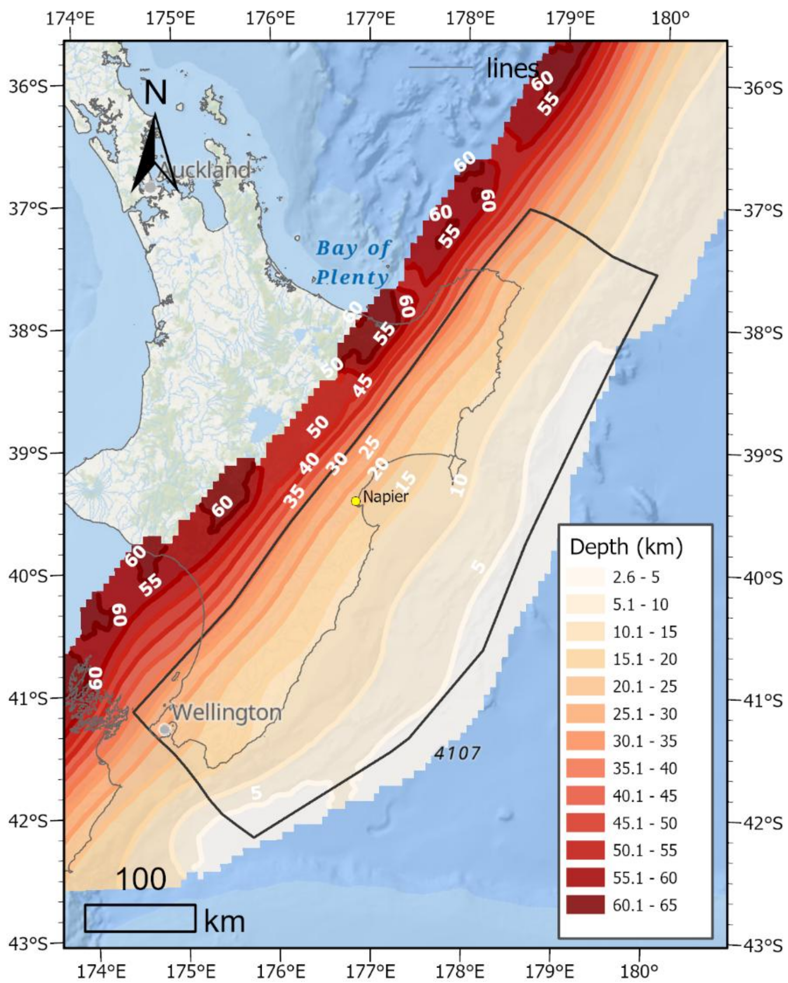

Figure S2: Revised Hikurangi subduction zone interface model after Williams et al. (2013). The model is represented as a depth contour plot in this figure. Each contour is labelled with its depth value (km). The black outline describes the validity region of the model.

Subduction zone earthquake recurrence

Earthquake magnitudes within the HSZ are described by the Gutenberg–Richter relationship:

$$log\lambda_m = a - bm \quad \text{(S1)}$$

Where λ is the mean annual rate of exceedance, m is the magnitude, a is the rate of earthquakes expected in a region and b is the relative ratio of the different magnitudes The b-value represents the decay rate of the exponential distribution of events (where a high b-value indicates a relatively high proportion of small events and vice-versa).

The recurrence of the events in the subduction zone are implemented as suggested in the 2022 update of the New Zealand National Seismic Hazard Model (Gerstenberger et al, 2022; Rollins et al, 2022).

The dimensions of the floating ruptures generated across the margin follow the scaling relationships in Strasser et al (2010). This implementation was made using the OpenQuake software (GEM 2019) and ground motions were obtained using GMPEs for each individual event as described in the scenario section for the subduction zone events. The investigation time consists of 100,000 stochastic event sets of 1 year duration. The Gutenberg-Richter (GR) plot of the synthetic catalogue of earthquakes on the HSZ is shown in Figure S2.

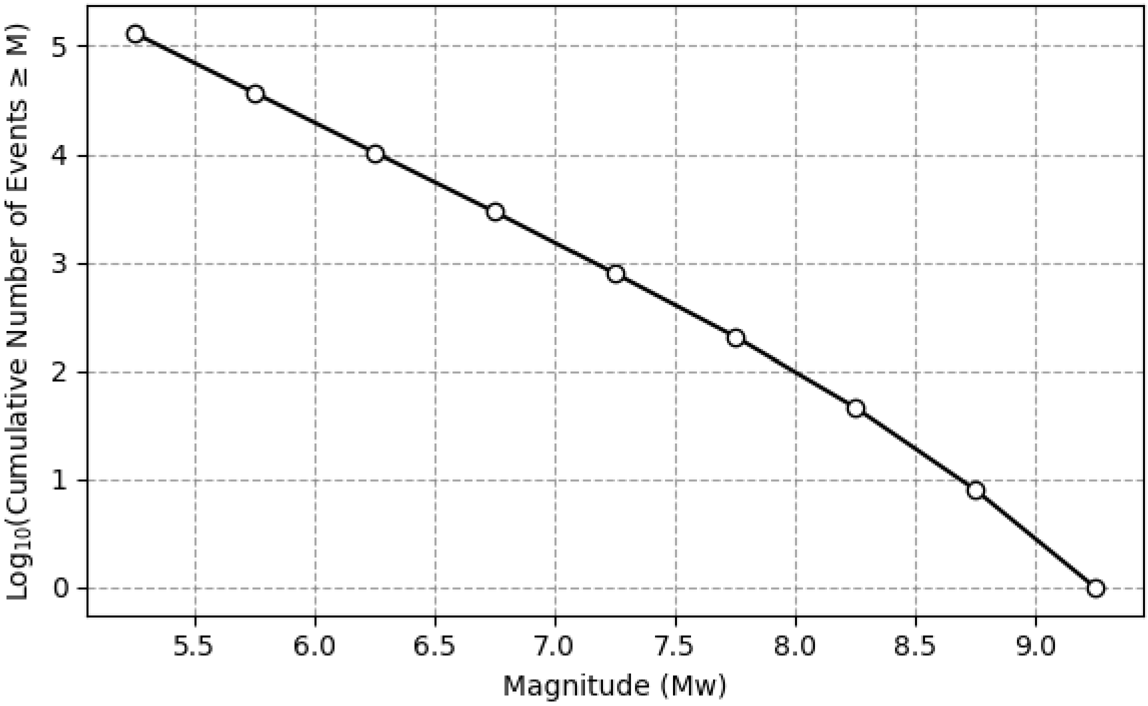

Figure S3: Gutenberg-Richter plot of the synthetic catalogue modelled in this study for the Hikurangi SZ. The plot shows the logarithm (base 10) of the cumulative number of earthquakes (N ≥ Mw) versus earthquake magnitude (Mw).

Ground motion modelling

Ground Motion Prediction Equations (GMPEs) for subduction interface events were selected following the New Zealand Seismic Hazard Model recommendations (Gerstenberger et al., 2022). Site effects were incorporated through the mean shear-wave velocity of the upper 30m (Vs_{30}).

For a reference location in Napier (latitude = –39.4786, longitude = 176.89617), an Annual Exceedance Probability (AEP) hazard curve was derived for a rock reference site using OpenQuake(Figure S3). Note that this hazard curve was calculated only for earthquakes on the HSZ that are included in this study and is therefore not an estimate of the total seismic hazard at that point. The latter would need to include the seismic hazard from earthquakes generated on other faults as well.

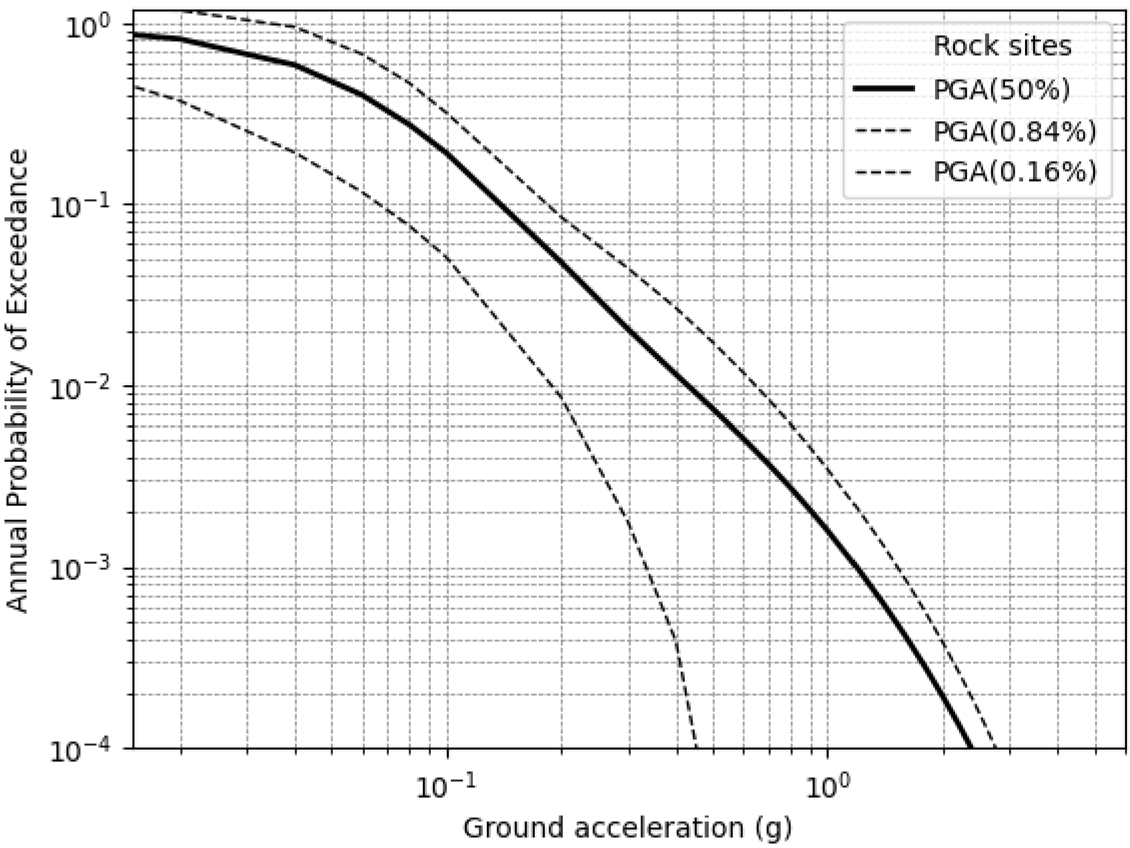

Figure S4: Reference rock Annual Exceedance probability (AEP) hazard curves in Napier (lat=-39.4786, lon= 176.89617) for Peak Ground Acceleration (g) at 16%, 50% and 84% percentiles, for earthquakes on the HSZ interface.

S3. Tsunami hazard modelling

Stochastic Source Models and Simulated Scenarios

The methodology we used to simulate slip distribution on the rupture interface follows that described by Geist (2002), which in turn is based on the method suggested by Herrero and Bernard (1994). Bernard et al. (1996) demonstrated that a self-similar mode of rupture is expressed in ω2 falloff in the seismic source spectrum for frequencies higher than a corner frequency. This characteristic of the seismic signal can be related to a k2 decay in the radial wave number spectrum of the slip distribution (Aki, 1967; Andrews, 1980; Herrero and Bernard,1994). Wave numbers less than a corner wave number kc do not scale in this fashion and are kept constant. The corner wave number kc varies with the characteristic rupture dimension and therefore the magnitude of the earthquake. Herrero and Bernard (1994) used kc=1/L where L is the fault dimension. The stochastic model is created by keeping a constant phase for k<kc and randomizing it for higher wave numbers (k>kc).

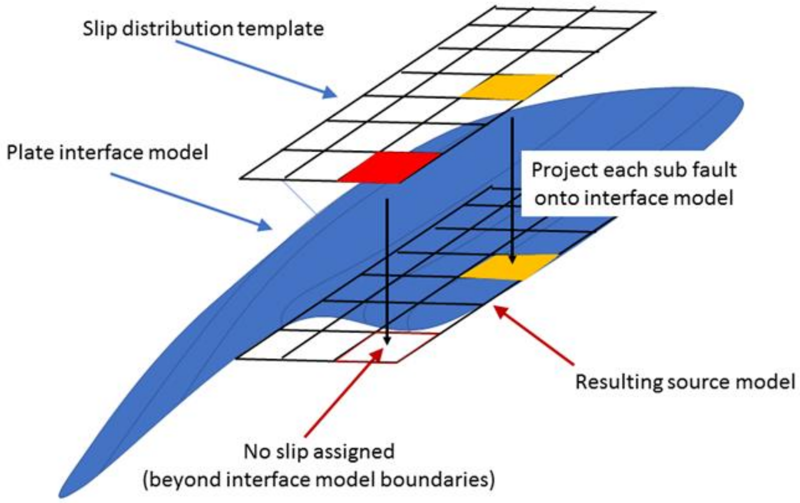

Figure S5: Illustration of the method to create a non-uniform slip subduction interface model. A stochastic non – uniform slip distribution is calculated for a template rectangular finite fault model with a regular grid. From the approximate position of this template position, dip and strike are found on the subduction zone geometric model. The model is represented by a set of rectangular Okada (1985) sub-faults in the format needed for the tsunami simulation code. The geometry of the template fault is taken from Open Quake outputs. The blue surface represents the subduction zone interface in this illustration.

Slip distributions are first calculated on a rectangular finite fault source template (slip distribution template, Figure S5) its overall position, strike and dip are taken from the OpenQuake sources. We are restricted to using rectangular subfaults in our projection onto the subduction surface due to current limitations in the algorithm that calculates the surface deformation resulting from this slip distribution (Okada, 1985). The subfault dimensions are set to be the shallowest depth of the resulting source. In this approach we project subfaults vertically directly onto the interface model. Where the interface is not defined no subfaults are added to the final source.

The seismic moment is set as requested for the source to be simulated. The final model is scaled to the correct moment by increasing slip overall appropriately. With this scaling we compensate for subfaults that could not be projected onto the interface from the original source template. This approach can create shallow (close to the trench) non-uniform slip sources on the interface model but is not suited for sources that cover steeply dipping parts of the interface.

For each slip distribution we then modelled the initial deformation, tsunami propagation and resulting inundation into Napier using ComCOT (Cornell Multi-grid Coupled Tsunami model), a model progressively developed during the mid-90s at Cornell University and then continuously developed at GNS Science, New Zealand, carefully tested and widely applied to numerous tsunami studies (e.g. Liu et al., 1995; Wang & Power, 2011; Wang et al., 2020; Roger et al., 2023; Roger and Wang, 2023). It computes tsunami generation, propagation, and coastal interaction by solving both linear and non-linear shallow water equations using a modified explicit leap-frog finite difference scheme and considering the weak dispersion effect (Wang, 2008). The initial sea surface deformation is calculated using the Okada (1985)'s formulae with the fault plane geometry and either a uniform or non-uniform slip distribution. Water surface elevation and horizontal velocities are calculated respectively at the cell centre and at the edge centres of each grid cell of the computational domain. Absorbing boundary schemes are used at the boundaries of the computational domain to dampen the incoming waves, avoiding reflection from the grid boundaries. The DEM used for the present study is the same one used in a previous tsunami inundation study for Napier (Fraser et al, 2014).

In total 330 tsunami inundation simulations of Napier were completed for this study and the flow depths at each building in each model for each scenario was extracted. Due to the spatial resolution of the simulation domain (~10 m), and the extent of many buildings (≤ 10m), a buffer zone of 10 m wide was drawn around each building to help the extraction of flow depth values. Figure S6d shows the spatial distributions of buildings in Napier City exposed to tsunami hazard from at least one scenario in the library.

In Figure S6a we show the probabilistic tsunami inundation hazard, expressed as a flow depth values, at 8 locations (Figure S6b) corresponding to specific building locations extracted from the New Zealand buildings outlines shapefile (LINZ, https://data.linz.govt.nz/layer/101292-nz-building-outlines-all-sources/). These 8 sites were selected after analysis of the flow depth maps produced as outputs of tsunami simulation: locations where the tsunami waves inundate urban areas the most frequently were selected.

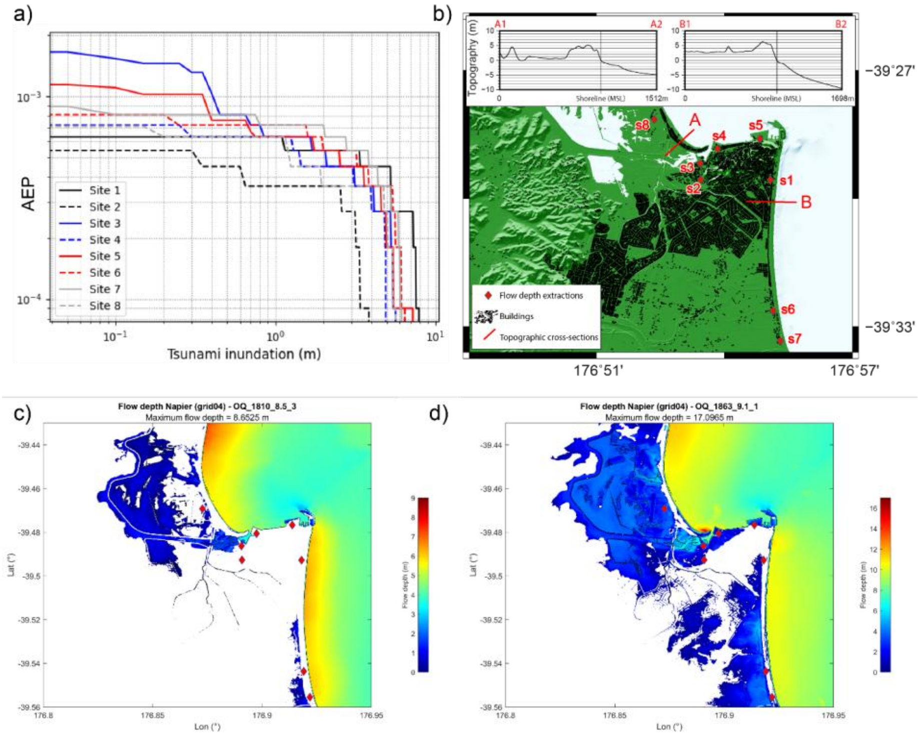

Figure S6: a) Annual Exceedance probability (AEP) hazard curves for tsunami inundation depths for the 8 selected sites in Napier City. b) Napier 10 m resolution DEM used for the inundation simulation in the present study. The building footprints are symbolized with black contours; the red diamonds locate the 8 locations of flow depth extractions shown in (a); the red segments represent the 2 topographic cross-sections along the coast (A & B); c) and d) show the flow depth maps for 2 different scenarios (Mw 8.5 and Mw 9.1) considered in the AEP hazard curves construction.

The tsunami hazard curves show two different bumps or steps at ~0.3-0.5 m and ~4-6 m flow depths (See Figure S6a). These two steps can be explained by looking into detail at the coastal topography of Napier and the different tsunami simulation output results. The first step is due to tsunami inundation via the river estuaries, and particularly the Ahuriri River estuary located in the coast of the town, which generally has a very flat topography (Figure S6b) and where all simulated tsunamis penetrate, including the smallest simulated tsunamis, which do not reach any buildings (e.g., Figure S6c). If the flow depth is sufficient to overtop the banks of the estuary, whose minimum altitude lies approximately within 0.3-0.5 m above mean sea level, then the water begins to inundate the built environment. As this is not the case for all the tested scenarios, the AEP decreases abruptly at these flow depths. The second one corresponds to the 4-6 m high barrier-beach gravel ridge located along the east coast of the town(Figure S6b). The simulation of the largest scenarios show that a large part of the town is inundated only if the tsunami waves overtop this natural coastal protection (Figure S6d). This corresponds to 8/330 simulated scenarios of magnitude Mw 8.9-9.1 which leads to another and more abrupt decrease of the AEP.

As mentioned in the main text, tsunamis triggered by submarine landslides occurring as a result of ground shaking have also not been considered in the present study. However, the bathymetry offshore Napier shows (1) many underwater landslides evidence as it is the case along the whole eastern continental margin of New Zealand (Roger et al., 2024); and (2) numerous underwater canyons along the slope of the North Island continental margin, including large canyons systems like the Poverty Canyon System off Mahia Peninsula, northern Hawke's Bay (Mountjoy, 2009), which sediment cover may be destabilized during an earthquake shaking. Scholz et al. (2016) demonstrated that ground acceleration accompanying earthquakes (even large ones of Mw 8.0+) is not enough to trigger sediment destabilization (they use the example of the Cascadia Margin case, relatively similar to the Hikurangi Margin case): they observed that the sediment frictional resistance must be significantly reduced, conditioned with sea level variations, rapid sedimentation rate, etc., to allow earthquake to trigger submarine landslides. Deeper analysis of the sediment context offshore New Zealand is needed before these secondary tsunami sources could be incorporated into studies such as this one.

For this study we have also not included the effect of debris on the damage from the tsunami. Debris impact loading associated with tsunami waves is particularly important to consider in many cases as shown during the large tsunami of Indonesia in 2004, Chile in 2010 or Japan in 2011 (e.g., Fraser et al., 2013; Naito et al., 2014; Nistor and Palermo, 2015). These debris can result directly from the destruction of infrastructures, but tsunami waves inundating port facilities can also carry boats, containers, timbers, etc., which will add additional consequences on structures located onshore, sometimes leading to their collapse (Como and Mahmoud, 2013). Napier hosts the fourth largest port of New Zealand in terms of container volume (Curtis and Pohlen, 2019). There are often many timbers and containers stored on the storage depot, an area identified in several scenarios of the present study as potentially inundated during a tsunami event. Many studies have been led to simulate the debris carried by tsunami flow (e.g., Conde et al., 2015; Park et al., 2021; Chida and Mori, 2023). However, they do not provide a way to determine whether a building can further become debris. Kaida and Kihara (2020) propose a methodology using both Probabilistic Tsunami Hazard Assessment (PTHA) and Tsunami Fragility Assessment (TFA) on structures to evaluate the annual failure frequency of these structures. This methodology could potentially be further applied to Napier to improve the assessment of earthquake cascading hazards when they cause a tsunami in future work.

S4. Liquefaction hazard modelling

Selection of liquefaction intensity measure

Different approaches have been derived by different authors for quantifying the expected effects associated with liquefaction displacements. Liquefaction Resistance Index (LRI; Cubrinovski et al, 2011), liquefaction potential Index (LPI Iwasaki et al, 1978), One-Dimensional Volumetric Reconsolidation Settlement (SV1D, Tonkin & Taylor, 2013) and Liquefaction Severity Number (LSN, Tonkin & Taylor, 2013) are examples of the most commonly used parameters for liquefaction analysis. LSN has been shown to best correlate with the likelihood of vertical differential ground surface subsidence occurring away from lateral spread areas, and is a better estimate for the prediction of flat land liquefaction damage (e.g. land where built infrastructure may be located, (Tonkin & Taylor, 2013; van Ballegooy et al. , 2014; van Ballegooy et al;., 2015; Tonkin & Taylor 2015; Griffin and Dellow 2020; Griffin et al. 2020, Griffin 2024))

LSN is calculated as the integration of the volumetric densification strain (εv or deformation expected in the liquefiable layers) of the first 10 m of soil (z), as presented in Equation (2).

$$LSN = \int_0^{10} \varepsilon vz \, dz \quad \text{(S2)}$$

Here, εv is assessed from liquefaction triggering analysis (Robertson & Wride, 1998; Boulanger RW & Idriss IM, 2014; Bouziou et al., 2019). The method is an empirical relationship that combines the cone penetration test (CPT) CPT tip resistance (qc), CPT sleeve friction (fs), soil behaviour type index (Ic), cyclic resistance ratio (CRR) and cyclic stress ratio (CSR) to calculate the factor of safety against liquefaction (FS) and estimate the volumetric strain of the soil, ε. Then, ε is combined with the thicknesses of the different sublayers subjected to liquefaction to estimate LSN as described in Equation 2.

Liquefaction triggering is a function of the ground shaking level and the earthquake magnitude. As liquefaction is only expected in saturated soils, summation is only made for layers below the ground water table. More details on the above can be found in the literature (Tonkin & Taylor, 2013; van Ballegooy et al., 2014; van Ballegooy et al; 2015; Tonkin & Taylor 2015).

The liquefaction susceptibility of a soil is dependent on its compositional characteristics and state in the ground, for example the age and geological environment. Soils that are cohesive (e.g., clays with high plasticity) are not susceptible to liquefaction (Idriss and Boulanger 2008). Liquefaction is triggered in a susceptible soil layer if the soil is saturated and the level of shaking is sufficiently large enough to overcome the soil's resistance to liquefaction (Rosser and Dellow 2017).

Liquefaction Severity Number (LSN) modelling in Napier

Rosser and Dellow (2017) used surface geomorphological and sedimentological maps on top of a subsurface borehole database to compile areas of similar geomorphic age and origin that may be prone to liquefaction across Hawkes Bay. In particular, Napier City was divided into six liquefaction susceptibility zones using the liquefaction susceptibility estimation criteria in Boulanger and Idriss (2014) and the geological and sedimentological properties mapped in the area. Five hundred and ninety (590) cone penetration tests (CPTs) were grouped by their geomorphic zone, and the top 10 metres were quantitatively analysed following the approach used by Tonkin & Taylor (2013).

To improve the liquefaction dataset, 17 CPTs located in four of the geomorphic zones based on the LSN groupings in Rosser and Dellow (2017) were analysed by Griffin (2024), to reduce the uncertainty of those liquefaction zones of Rosser and Dellow (2017). These site-specific CPTs were chosen based on being >5m deep, having digital CPT data available to analyse, and having a groundwater level associated with them. Data were uploaded into and checked using GeoLogismiki's CPeT-IT software, before inputting the data into Cliq liquefaction-triggering assessment software (also by GeoLogismiki). For each CPT, the software's default input parameters were applied, and were assessed using the liquefaction triggering criteria outlined in Boulanger and Idriss (2014) and Rosser and Dellow (2017). Earthquake magnitudes (Mw) intervals of 0.1Mw and peak ground accelerations

(PGA) intervals of 0.05g were adopted to build an LSN database that captures the variability of LSN at each susceptibility area under the possible range of earthquake conditions in the synthetic catalogue.

For a given PGA, the expected LSN distribution is defined by the mean and standard deviation calculated for each CPT within each susceptibility zone, assuming a normal distribution. LSN is directly proportional to the level of shaking (PGA) and the earthquake magnitude, until maximum volumetric strain, ε, is reached. Figure S7 presents PGA and LSN distributions for three sample earthquake scenarios analysed, along with the LSN hazard curves in the same liquefaction zone. Results for all 6 zones are shown.

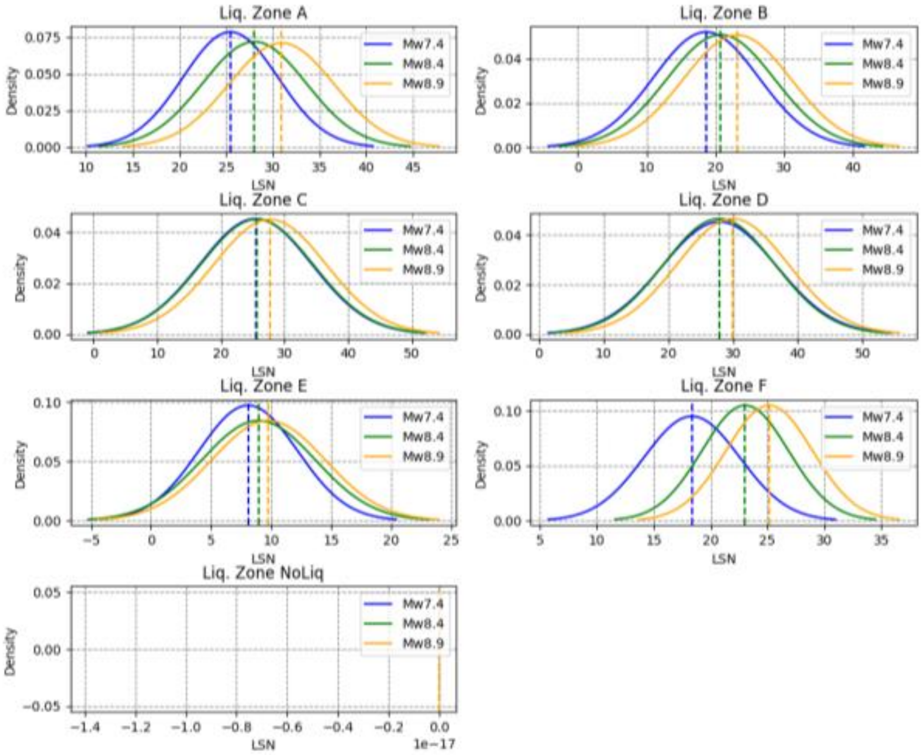

Figure S7: LSN distributions across the modelled liquefaction susceptibility zones. The corresponding PGAs and magnitudes for each of three example earthquake scenarios are displayed. Vertical dashed lines indicate the median PGA for each event.

S5. Lateral spreading hazard modelling

Liquefaction-induced lateral displacements (LD) were estimated following the method proposed by Zhang et al., (2004). This approach first involves calculating the Lateral Displacement Index (LDI) and then incorporating the effects of ground slope, both with and without the presence of a free face. The LDI is obtained by integrating the maximum amplitude of cyclic shear strains (ϒmax), which are derived from CPT-based empirical relationships, over the thickness of the liquefiable soil layer (zmax):

$$LDI = \int_0^{zmax} \Upsilon dz \quad \text{(S3)}$$

Both ϒmax and the thickness of liquefied layers depend on soil properties and earthquake characteristics. For a site with a ground slope (S) but without a free face, the lateral displacement is estimated using:

$$LD = (S + 0.2)LDI \; (for\ 0.2\% < S < 3.5\%) \; \text{(S4)}$$

By contrast, for a site with a free face, the lateral displacement is determined based on the ratio of the distance from the free surface (L) to its height (H), as follows:

$$LD = 6\left(\frac{L}{H}\right)^{0.8} LDI \ (for\ 4 < \frac{L}{H} < 40) \quad \text{(S5)}$$

This procedure was applied to compute LDI values at each CPT location across the liquefaction susceptibility zones identified within Napier City. During the Canterbury Earthquake Sequence (CES), areas situated within 240 m of water bodies were observed to have experienced lateral displacements exceeding 0.5 m (Cubrinovski et al. 2012), corresponding to a 'severe' damage state in SYNER-G (Pitilakis et al. 2014).

In this study, to model lateral spreading-induced damage to road segments, the distance to the nearest free face (L) was determined for each road segment within a 240 m buffer. A 1 m resolution Digital Elevation Model (DEM) was used to derive the mean free-face height (H) along watercourses at 10 m intervals. The same DEM was also used to generate a slope map and to calculate the mean slope percentage (S) between the nearest free face and each 50 m road segment.

Finally, LDI values were adjusted in areas with gently sloping ground lacking a free face or in level areas with a free face, using Equation A4.2 and Equation A4.3, respectively (Zhang et al. 2004).

S6. Landslide hazard modelling

The modelling of co-seismic landslide sources and debris runouts are summarised in the following steps:

1. The probability of co-seismic landsliding was modelled using the earthquake-induced landslide forecast tool for New Zealand: Version 2.0 (Massey et al., 2021b, 2022). The forecast tool is a statistical model that predicts the spatial distribution of earthquake induced landslide probability over an area at the regional scale. In this study, the tool was used to estimate the susceptibility of a slope to generating landslides, and the landslide intensity, at different levels of earthquake ground shaking (PGA). The tool was run 10 times using the uniform input PGA values of 0.2g, 0.3g, 0.4g, 0.5g, 0.75g, 1g, 1.5g, 2g, 2.5g, 3g. This span of PGA values represents the range of possible ground shaking likely to produce earthquake-induced landsliding from the maximum earthquake modelled in the stochastic catalogue (i.e., a Mw9.1 HSZ earthquake)
2. To define the maximum extent of a landslide source, which is not an output of the earthquake-induced landslide forecast tool, we delineated slope units which represent slope facets. An iterative process was used to create and refine the slope units. Within the Napier area of interest, all slopes ≥ 10 degrees were identified using the NZ 8m Digital Elevation Model (https://data.linz.govt.nz/layer/51768-nz-8m-digital-elevation-model-2012/). The 8m DEM was chosen over a higher resolution lidar DEM to remove the effects of local topographic features at the sub-hillslope scale. Due to the low resolution of the 8 m DEM which smooths topographic features, we used a slope threshold of 10 degrees to distinguish hillslopes from the flat terrain. All slopes >10 degrees were then separated into slope units by removing cells with divergent flow along ridgelines and prominent spurs running down between the hillslope faces. These divergent cells were removed from the slope units, leaving a gap between adjacent slope units, as the landslide runout direction is ambiguous for these locations. Additionally, manual editing of the individual slope units was required to divide the larger, whole of catchment slope units into hillslope facets either side of the main channel divide (Figure S8a).
3. To represent the potential landslide locations more accurately, source regions were determined using empirical relationships between slope, local slope relief (LSR) and landslide occurrence (Brideau et al.

2020, Massey et al. 2021a). These empirical relationships were determined from the co-seismic landslide inventory for the 2016 Mw 7.8 Kaikōura earthquake (Jones et al., 2024), which occurred in the east coast of the South Island of New Zealand and contains <30,000 landslides. To capture the influence of local topographic features, the creation of source regions used a 3m lidar DEM covering the Napier study area (https://data.linz.govt.nz/layer/112889-hawkes-bay-lidar-1m-dem-2020-2021/). As the lidar DEM is higher resolution, we increased the slope angle threshold to ≥20 degrees, as co-seismic landslides rarely occur on slopes < 20 degrees within New Zealand, to determine the maximum credible volume class (Table 2). This is calculated as the difference in elevation between the lowest elevation within an 80 m radius from the centroid of the given sample grid cell and the mean elevation of that grid cell. A polygon was created for each landslide volume class, up to the maximum credible volume, and these polygons were clipped to the extent of the slope units (Figure S8b).

4. For each landslide volume class, within each source region, the probability of earthquake induced landsliding for each PGA scenario was summed using the underlying values predicted from the earthquake-induced landslide forecast tool. We then determined the probability of the landslide volume class occurring within the source regions using the Kaikōura landslide inventory.

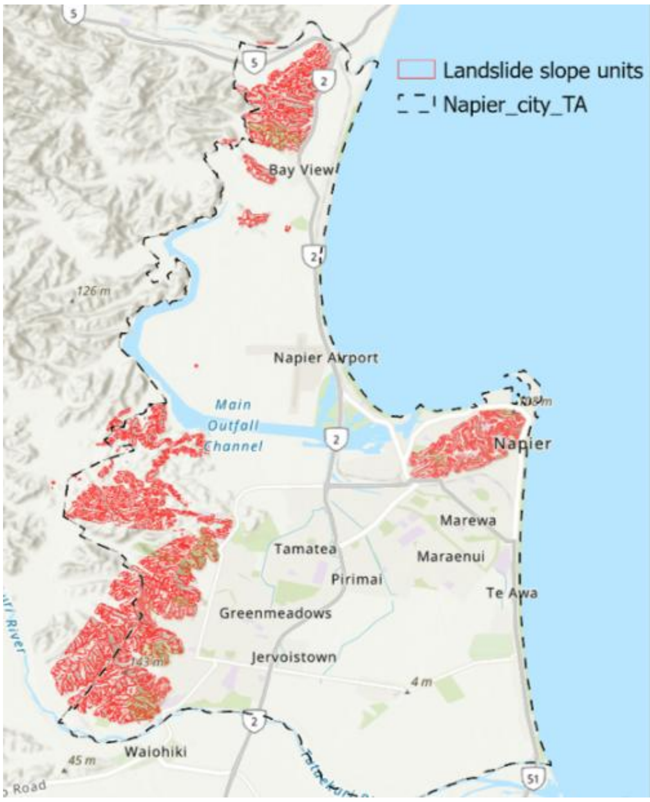

Figure S8 Slope units created for the Napier AOI. The slope units were used to define hilly areas were co-seismic landslides might occur.

Table S1. Landslide volume classes used in the landslide risk assessment. The probability of a landslide of a given volume class occurring within each source region was determined using the landslide frequency versus source area relationship taken from the Kaikōura earthquake landslide inventory (Version 3.0; Jones et al. 2024). The landslide inventory displays a 'roll over' in the distribution at a source area of ~500 m2 in the frequency – source area relationship. The equivalent source area volume falls between landslide volume classes (1) and (2), indicating that the number of smaller landslides (with source areas <500 m2) are under-represented in the distribution. Therefore, for volume class (1), it is assumed that PVOL is 50% of the sum of volume classes (1) and (2) combined. The Fahrböschung angle for a given landslide volume class based on a compilation of a global dataset of landslides from academic papers and reports where these parameters are reported (Brideau et al. 2021a, 2021b).

Landslide Volume Class	Volume (m3)	Area (m2)	LSR 80 mean (m)	OSD Fahrböschung P50	Obstacle	Data from the V3.0 Kaikōura EIL Inventory		
						Number of Landslides	Proportion of Landslides	Assumed Probability of an EIL Occurring (PVOL)
1	3	3	3	43.79	0			
2	32	30	50	41.62	0	12,583	40%	0.4390
3	316	200	60	39.46	0.5	15,184	48%	0.4390
4	3,162	1,600	71	37.33	1	3,477	11%	0.1100
5	31,623	12,000	87	27.57	1	337	1%	0.0107
6	316,228	89,000	100	20.88	1	32	0.1%	0.0010
7	3,162,278	675,000	100	43.79	1	10	0.03%	0.0003

5. The landslide runout from each volume class, up to the maximum credible volume class, were modelled in ArcGIS using a set of empirical relationships based on observations of landslides in New Zealand and worldwide (Brideau et al. 2021a; Brideau et al. 2021b). Debris inundation relationships have been established for these three types of landslides initiated under ‘dry’ or ‘wet’ conditions; these being: (1) open slope dry rock and debris avalanches (OSD); (2) open slope wet debris avalanches (OSW), and (3) channelized wet debris flows (CHW). As OSD rock and debris avalanches are frequently triggered by earthquakes, while OSW debris avalanches and CHW debris flows are more likely triggered by rainfall. Thus, only OSD rock avalanche relationships were used in this study. The landslide debris inundation extents modelled here were estimated based on the 50% runout Probability of Exceedance (POE) extent for a landslide type of a given volume. This assumes that in 50% of cases, the landslide debris would extend further than estimated, and that in 50% of cases the landslide debris would extend less than estimated.
6. The empirical debris inundation relationships use the Fahrböschung angle, which is the angle between the landslide source and the landslide deposit using the ratio of elevation difference and horizontal distance between the crest of the landslide source and distal toe of the deposit. For each volume class, up to the maximum credible volume class within each slope unit, the Fahrböschung angle was estimated from Table 2. In ArcGIS, using a 3m lidar DEM covering the Napier study area (LINZ a, b; 2024), the Fahrböschung angle was projected as the maximum distance for runout from each cell within the slope

unit for each landslide volume class which captures the maximum area for inundation because it models every possible runout direction.

7. Buildings which intersect the source region and/or runout polygon for each landslide volume class were extracted and stored for use in the later MCS analysis.

S7. Exposure modelling

The national building inventory compiled by Scheele et al. (2023) integrates three datasets to characterise both residential and non-residential structures.

- Property rating valuation data from CoreLogic provided attributes such as use category, age, and wall material, which were adjusted for compatibility with fragility and vulnerability models.
- Building outlines from LINZ were linked to property parcels using LINZ primary property parcels data.
- Point location data were matched to building outlines within the same parcel, following the matching logic described by Scheele et al. (2023), primarily using floor area to ensure consistency between point and polygon records.

From this national dataset, 38,344 residential buildings were identified within the Napier City Territorial Authority boundary. Figure S9 shows the spatial distribution of building exposure, expressed as the percentage of total replacement value (%RV) across the study area. Figure S10a-d shows the buildings exposed to liquefaction, lateral spreading, landslides and tsunami respectively.

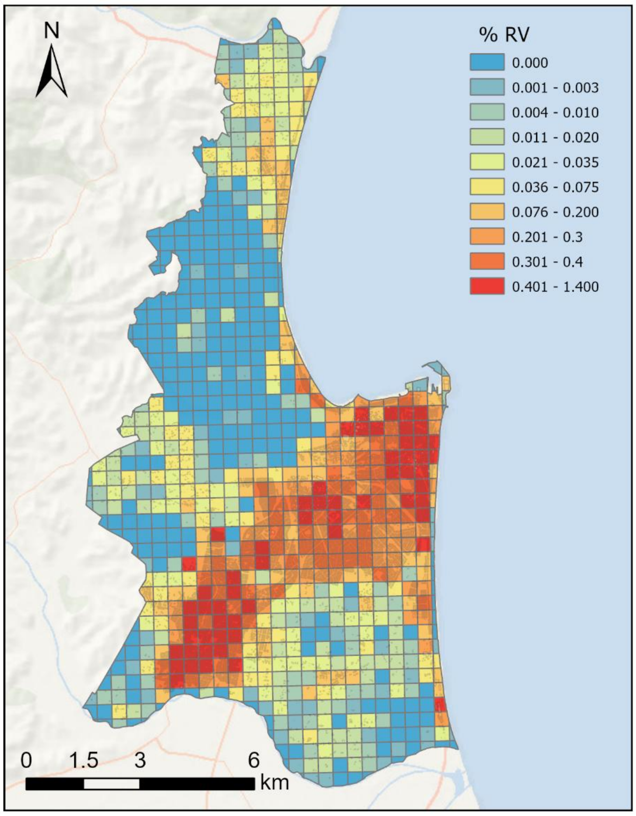

Figure S9: Building value distribution in Napier City, expressed as the percentage of the total replacement value within the case study area (% RV) in the exposure dataset.

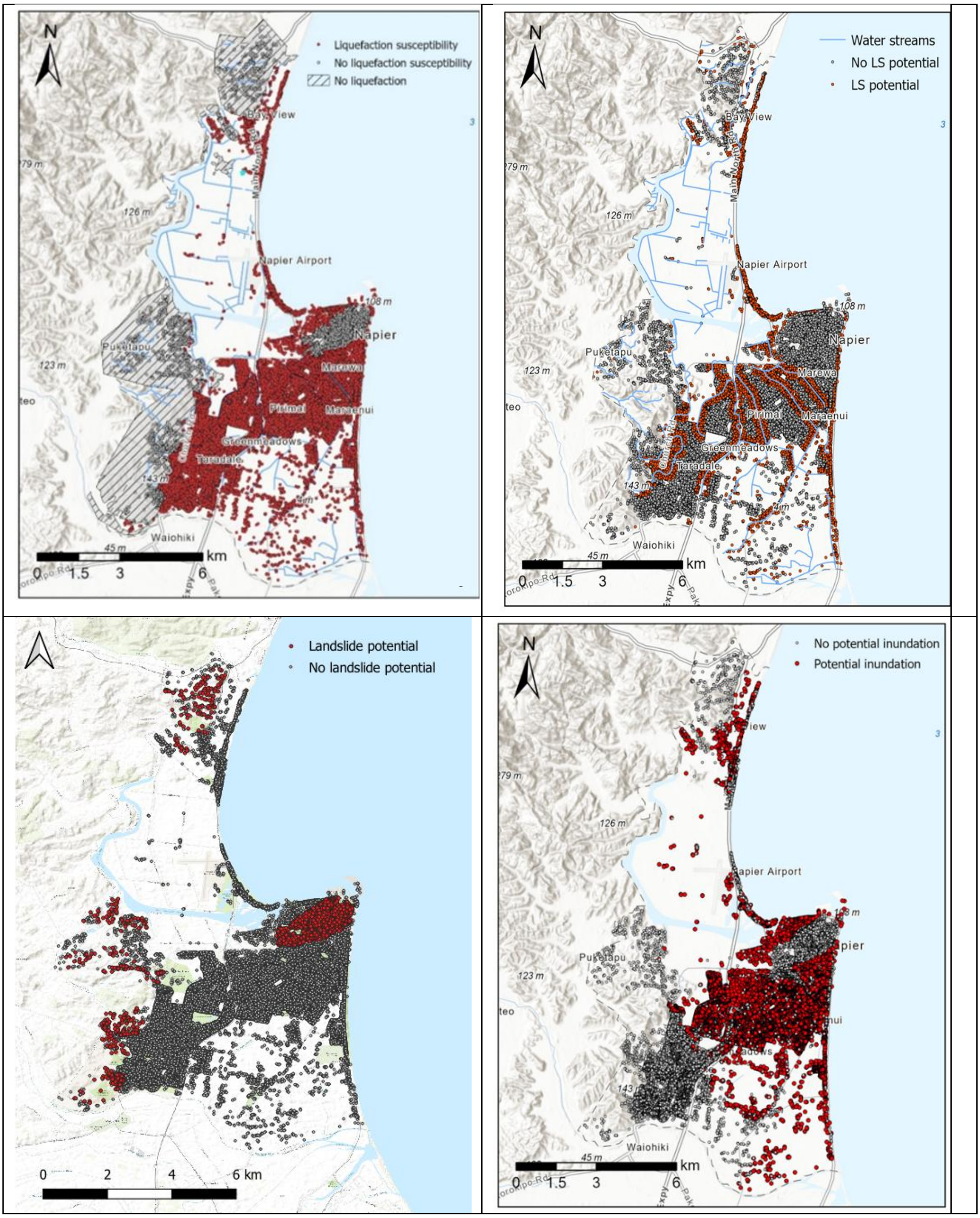

Figure S10: Buildings in the region that are potentially exposed to impacts from a) liquefaction b) lateral spreading c) landslide and d) tsunami inundation

S8. Fragility/vulnerability modelling

To enable consistent assessment of structural performance under multiple hazards, this study defined a harmonized five-level damage state (DS) framework.

Each hazard—earthquake shaking, liquefaction, tsunami inundation, lateral spreading, and landslides—can produce different physical damage mechanisms and degrees of functional loss. Therefore, a unified scale was established to integrate results across all perils within a common structural loss framework.

This approach follows the conceptual basis used in HAZUS (FEMA, 2020) and similar multi-hazard studies (e.g., Rossetto & Elnashai, 2003; FEMA P-58, 2012; Supprasri et al., 2013; Koshimura & Suppasri, 2015).

The harmonized damage states (DS1–DS5) describe the physical extent of structural and non-structural damage, associated functionality loss, and corresponding repair requirements.

DS1 – Slight:

Characterized by superficial or non-structural effects. Examples include fine plaster or drywall cracking, minor ceiling deformation, and light detachment of cladding or finishes caused by low-level earthquake shaking. In liquefaction or lateral spreading conditions, this corresponds to negligible surface settlement (<5 cm) or minor ground deformation without structural impact. For tsunami inundation, slight water intrusion without structural damage may occur (e.g., minor flooding of non-critical spaces). Landslide impacts correspond to absence of debris near the structure. Functionality is fully retained, and no structural repair is required (Adapted from FEMA, 2020; Rossetto & Elnashai, 2003).

DS2 – Moderate:

Represents localized but repairable damage, such as larger cracks in infill or shear walls, detachment of non-structural components, or light yielding in ductile members due to seismic loads. For liquefaction, this includes small differential settlements (5–15 cm) or minor foundation displacement. For lateral spreading, limited footing rotation or displacement may occur. Under tsunami loading, light hydrostatic or hydrodynamic pressure may cause partial water intrusion and minor wall deformation. Landslide debris may partially affect the building perimeter. The structure remains safe for occupancy after limited repairs. (FEMA, 2020; Supprasri et al., 2013; Rossetto & Elnashai, 2003).

DS3 – Severe:

Corresponds to major structural distress with significant loss of stiffness or strength. Examples include diagonal cracking, partial shear failure, spalling of concrete cover, or residual drift exceeding serviceability limits. Liquefaction effects may include severe lateral spreading (>30 cm), tilting, or partial bearing failure. Tsunami impacts may cause large pressure-induced cracking or collapse of weak walls, while landslide activity could induce foundation destabilization. The building's structural integrity is compromised, though collapse is not imminent. Extensive repairs or partial replacement of load-bearing elements are required. (FEMA P-58, 2012; Supprasri et al., 2013; Koshimura & Suppasri, 2015).

DS4 – Complete:

Denotes near or full structural failure of primary load-resisting components. This includes soft-story or cripple-wall collapse, column shear failure, or global instability caused by severe ground motion or permanent deformation. In liquefaction or lateral spreading cases, foundations may experience major displacement or settlement (>50 cm), leading to uninhabitable conditions. For tsunami events, strong hydrodynamic forces and debris impact can cause partial structural collapse or wall failure, while landslide runout may bury or crush portions of the building. The structure is uninhabitable and requires full reconstruction or major retrofitting. (FEMA, 2020; Rossetto & Elnashai, 2003; Supprasri et al., 2013).

DS5 – Collapsed:

Represents total structural failure or complete destruction. This includes total building collapse due to seismic loading, foundation loss from liquefaction or lateral spreading, wash-away or complete scour from tsunami forces, or burial under landslide debris. No structural components remain functional, and the building must be entirely reconstructed. (FEMA P-58, 2012; Supprasri et al., 2013; Koshimura & Suppasri, 2015).

S9. References

Aki, K.: Scaling law of seismic spectrum, J. Geophys. Res., 72, 1217, doi:10.1029/JZ072i004p01217, 1967.

Andrews, D. J.: A stochastic fault model: 1. Static case, J. Geophys. Res., 85, 3867–3877, doi:10.1029/JB085iB07p03867, 1980.

Ansell, J. H., and Bannister, S. C.: Shallow morphology of the subducted Pacific plate along the Hikurangi margin, New Zealand, Phys. Earth Planet. Inter., 93, 3–20, doi:10.1016/0031-9201(95)03085-9, 1996.

Bernard, A. B., and Durlauf, S. N.: Interpreting tests of the convergence hypothesis, J. Econometrics, 71, 161–173, doi:10.1016/0304-4076(94)01699-2, 1996.

Bouziou, D., van Ballegooy, S., Storie, L., and O'Rourke, T. D.: Spatial correlations of underground pipeline damage in Christchurch: correlations with liquefaction-induced ground surface deformations and CPT-based liquefaction vulnerability index parameters, Report for UC Quake Centre, Christchurch, New Zealand, available at: http://resources.quakecentre.co.nz/wp-content/uploads/2019/09/0806109_FINAL_LiquefactionReport-1.pdf , 2019.

Boulanger, R. W., and Idriss, I. M.: CPT and SPT based liquefaction triggering procedures, University of California, Center for Geotechnical Modeling Report UCD/CGM-14/01, Davis, CA, available at: https://facultysand.engineering.ucdavis.edu/boulanger/wp-content/uploads/sites/71/2014/09/Boulanger_Idriss_CPT_and_SPT_Liq_triggering_CGM-14-01_20141.pdf , 2014.

Brideau, M. A., Massey, C. I., Lukovic, B., and Morgenstern, R.: Deterministic mapping of potential landslide debris inundation in the Kaikōura District, GNS Sci. Consult. Rep., 2019/102, Lower Hutt, New Zealand, 2020.

Brideau, M. A., de Vilder, S., Massey, C., Mitchell, A., and McDougall, S.: V1.0 empirical landslide runout relationships compiled from international examples for various landslide types, DesignSafe-CI, doi:10.17603/ds2-9qbx-n796, 2021.

Brideau, M. A., de Vilder, S., Massey, C., Mitchell, A., McDougall, S., and Aaron, J.: Empirical relationships to estimate the probability of runout exceedance for various landslide types, in: Understanding and Reducing Landslide Disaster Risk, Springer, Cham, doi:10.1007/978-3-030-60227-7_36, 2021.

Burbidge, D. R., Rhoades, D. A., Christophersen, A., Power, W. L., Lin, S.-L., and Becker, J. S.: Exercise injects for a Hikurangi Subduction Zone earthquake aftershock sequence, GNS Sci. Consult. Rep., 2019/130, 16 pp., 2019.

Chida, Y., and Mori, N.: Numerical modeling of debris transport due to tsunami flow in a coastal urban area, Coast. Eng., 179, 104243, doi:10.1016/j.coastaleng.2022.104243, 2023.

Como, A., and Mahmoud, H.: Numerical evaluation of tsunami debris impact loading on wooden structural walls, Eng. Struct., 56, 1249–1263, doi:10.1016/j.engstruct.2013.06.023, 2013.

Conde, D. A. S., Telhado, M. J., Viana Baptista, M. A., et al.: Severity and exposure associated with tsunami actions in urban waterfronts: the case of Lisbon, Portugal, Nat. Hazards, 79, 2125–2144, doi:10.1007/s11069-015-1951-z, 2015.

Cubrinovski, M., Hughes, M., Bradley, B., McCahon, I., McDonald, Y., Simpson, H., Cameron, R., Christison, M., Henderson, B., Orense, R., and O'Rourke, T.: Liquefaction impacts on pipe networks, Short Term Recovery Project No. 6, University of Canterbury Research Report 2011-04, Christchurch, New Zealand, available at: https://ir.canterbury.ac.nz/bitstream/handle/10092/10178/12639392_NHRP-STRP6-Report-v1.0-22DEC11%20with%20Cover.pdf, 2011.

Cubrinovski, M., Robinson, K., Taylor, M., Hughes, M., and Orense, R.: Lateral spreading and its impacts in urban areas in the 2010–2011 Christchurch earthquakes, N. Z. J. Geol. Geophys., 55, 255–269, doi:10.1080/00288306.2012.699895, 2012.

Curtis, C., and Pohlen, C.: Napier Port infrastructure condition assessments using GIS technology, in: Australasian Coasts and Ports 2019 Conference, Engineers Australia, Hobart, 263–266, 2019.

El Kortbawi, M., Green, R. A., Wotherspoon, L. M., and Van Ballegooy, S.: Insights into the liquefaction hazard in Napier and Hastings based on the 1931 Hawke's Bay earthquake, in: 13th Australia–New Zealand Conference on Geomechanics, Perth, 2019.

Fraser, S. A., Power, W. L., Wang, X., Wallace, L. M., Mueller, C., and Johnston, D. M.: Tsunami inundation in Napier, New Zealand, due to local earthquake sources, Nat. Hazards, 70, 415–445, doi:10.1007/s11069-013-0820-x, 2014.

Fraser, S., Raby, A., Pomonis, A., Goda, K., Chian, S. C., Macabuag, J., Offord, M., Saito, K., and Sammonds, P.: Tsunami damage to coastal defences and buildings in the 11 March 2011 Mw 9.0 Great East Japan earthquake and tsunami, Bull. Earthq. Eng., 11, 205–239, doi:10.1007/s10518-012-9348-9, 2013.

Geist, E. L.: Complex earthquake rupture and local tsunamis, J. Geophys. Res., 107, 2086, doi:10.1029/2000JB000139, 2002.

Geographx: 8 m digital elevation model 2012, available at: https://data.linz.govt.nz/layer/51768-nz-8m-digital-elevation-model-2012/, 2012.

Griffin, A. G.: Liquefaction analysis for selected locations in Napier–Hastings, GNS Sci. Rep., 2024/07, 2024.

Griffin, A. G., and Dellow, S.: Wellington City Council liquefaction data: review and recommendations, GNS Sci. Consult. Rep., 2020/08, 2020.

Griffin, A. G., Pradel, G. J., Abbott, E. R., and Hill, M. P.: Liquefaction susceptibility verification for Wellington City Council, GNS Sci. Consult. Rep., 2020/109, 2020.

Haidekker, S., Uytendaal, A., Hicks, A., Wade, O., Wade, H., et al.: Ngaruroro, Tutaekuri, Karamu River and Ahuriri Estuary catchments state and trends of river water quality and ecology, Hawke's Bay Regional Council, Hawke's Bay, 2016.

Herrero, A., and Bernard, P.: A kinematic self-similar rupture process for earthquakes, Bull. Seismol. Soc. Am., 84, 1216–1228, 1994.

Hughes, M., Quigley, M., van Ballegooy, S., Deam, B., Bradley, B., Hart, D., and Measures, R.: The sinking city: earthquakes increase flood hazard in Christchurch, New Zealand, GSA Today, 25, 3–4, doi:10.1130/GSATG221A.1, 2015.

Iannacone, L., Otárola, K., Gentile, R., and Galasso, C.: Simulating multi-hazard event sets for life cycle consequence analysis, Nat. Hazards Earth Syst. Sci., 24, 1721–1740, 2024.

Idriss, I. M., and Boulanger, R. W.: Soil liquefaction during earthquakes, Monograph MNO-12, Earthquake Engineering Research Institute, 2008.

Inter-Agency Secretariat of the ISDR: Hyogo framework for action 2005–2015: building the resilience of nations and communities to disasters, United Nations ISDR, Geneva, 2007.

Iwasaki, T., Tatsuoka, F., Tokida, K., and Yasuda, S.: A practical method for assessing soil liquefaction potential based on case studies in Japan, in: Proc. Second Int. Conf. on Microzonation, 1978.

Kaida, H., and Kihara, N.: Fragility evaluation methodology for tsunami-borne debris impact, Coast. Eng. Proc., 36, 9–9, 2020.

LINZ: NZ 8 m digital elevation model 2012, [data set], available at: https://data.linz.govt.nz/layer/51768-nz-8m-digital-elevation-model-2012/, 2024a.

LINZ: Hawke's Bay LiDAR 1 m DEM 2020–2021, [data set], available at: https://data.linz.govt.nz/layer/112889-hawkes-bay-lidar-1m-dem-2020-2021/, 2024b.

Liu, P. L.-F., Cho, Y.-S., Briggs, M. J., Kanoglu, U., and Synolakis, C. E.: Runup of solitary waves on a circular island, J. Fluid Mech., 302, 259–285, doi:10.1017/S0022112095004095, 1995.

Massey, C. I., de Vilder, S. J., Lukovic, B., Townsend, D. B., and Rosser, B. J.: District-scale landslide risk analysis of debris inundation for the Kaikōura District, GNS Sci. Consult. Rep., 2021/89, 117 pp., 2021a.

Massey, C. I., Lukovic, B., Huso, R., Buxton, R., and Potter, S. H.: Earthquake-induced landslide forecast tool for New Zealand: version 2.0, GNS Sci. Rep., 2018/08, Lower Hutt, New Zealand, 77 pp., doi:10.21420/G2TP-9V, 2021b.

Massey, C., Lukovic, B., and Dellow, S.: A prototype Earthquake-Induced Landslide Forecast Tool for New Zealand, in: Coseismic Landslides: Phenomena, Long-Term Effects and Mitigation, Springer, Singapore, 617–631, doi:10.1007/978-981-19-6597-5_17, 2022.

Mountjoy, J. J. B.: Development of submarine canyon systems on active margins: Hikurangi Margin, New Zealand, PhD thesis, University of Canterbury, Christchurch, 271 pp., 2009.

Mueller, C., Burbidge, D. R., and Power, W. L.: Regional tsunami forecasting: uncertainties due to non-uniform slip, Pure Appl. Geophys., 178, 5155–5173, doi:10.1007/s00024-021-02845-5, 2021.

Naito, C., Cercone, C., Riggs, H. R., and Cox, D.: Procedure for site assessment of the potential for tsunami debris impact, J. Waterw. Port Coastal Ocean Eng., 140, 223–232, doi:10.1061/(ASCE)WW.1943-5460.0000222, 2014.

Nistor, I., and Palermo, D.: Post-tsunami engineering forensics: tsunami impact on infrastructure, in: Handbook of Coastal Disaster Mitigation for Engineers and Planners, Elsevier, 417–435, doi:10.1016/B978-0-12-801060-0.00020-4, 2015.

Okada, Y.: Surface deformation due to shear and tensile faults in a half-space, Bull. Seismol. Soc. Am., 75, 1135–1154, 1985.

Park, H., Koh, M. J., Cox, D. T., Alam, M. S., and Shin, S.: Experimental study of debris transport driven by a tsunami-like wave, Coast. Eng., 166, 103867, doi:10.1016/j.coastaleng.2021.103867, 2021.

Power, W. L., Burbidge, D. R., and Gusman, A. R.: The 2021 update to New Zealand's national tsunami hazard model, GNS Sci. Rep., 2022/06, doi:10.21420/X2XQ-HT52, 2022.

Robertson, P. K., and Wride, C. E.: Evaluating cyclic liquefaction potential using the cone penetration test, Can. Geotech. J., 35, 442–459, doi:10.1139/t98-017, 1998.

Robinson, T., and Rosser, N.: Rapid landslide risk assessment of transport infrastructure following the 2016 Kaikōura earthquake, EGU General Assembly, Vienna, 2017.

Roger, J., Pelletier, B., Gusman, A., Power, W., Wang, X., Burbidge, D., and Duphil, M.: Potential tsunami hazard of the southern Vanuatu subduction zone, Nat. Hazards Earth Syst. Sci., 23, 393–414, doi:10.5194/nhess-23-393-2023, 2023.

Roger, J. H. M., Bull, S., Watson, S. J., Mueller, C., Hillman, J. I., Wolter, A., Lamarche, G., Power, W., Lane, E., Woelz, S., and Davidson, S.: A review of approaches for submarine landslide–tsunami hazard identification and assessment, Mar. Petrol. Geol., 106729, doi:10.1016/j.marpetgeo.2024.106729, 2024.

Roger, J. H. M., and Wang, X.: Impact of tsunamis in Porirua Harbour: focus on Mana Marina, GNS Sci. Rep., 2023/31, doi:10.21420/WETZ-0X92, 2023.

Scholz, N. A., Riedel, M., Urlaub, M., Spence, G. D., and Hyndman, R. D.: Submarine landslides offshore Vancouver Island, Geo-Mar. Lett., 36, 323–337, doi:10.1007/s00367-016-0452-8, 2016.

Strasser, F., Arango, C., and Bommer, J.: Scaling of the source dimensions of interface and intraslab subduction-zone earthquakes with moment magnitude, Seismol. Res. Lett., 81, 941–950, doi:10.1785/gssrl.81.6.941, 2010.

Tonkin & Taylor: Canterbury earthquake sequence: increased liquefaction vulnerability assessment methodology, Report for the Earthquake Commission, Wellington, New Zealand, available at: https://www.eqc.govt.nz/ILV-engineering-assessment-methodology, 2015.

van Ballegooy, S., Wentz, F., and Boulanger, R. W.: Evaluation of CPT-based liquefaction procedures at regional scale, Soil Dyn. Earthq. Eng., 79, 315–334, doi:10.1016/j.soildyn.2015.09.016, 2015.

Wang, X.: Numerical modelling of surface and internal waves over shallow and intermediate water, PhD thesis, Cornell University, Ithaca, NY, 245 pp., 2008.

Wang, X., and Liu, P. L.-F.: An analysis of 2004 Sumatra earthquake fault plane mechanisms and Indian Ocean tsunami, J. Hydraul. Res., 44, 147–154, doi:10.1080/00221686.2006.9521671, 2006.

Wang, X., and Liu, P. L.-F.: An explicit finite difference model for simulating weakly nonlinear and weakly dispersive waves, Coast. Eng., 58, 173–183, doi:10.1016/j.coastaleng.2010.09.008, 2011.

Wang, X., and Power, W.: COMCOT: a tsunami generation, propagation and run-up model, GNS Sci. Rep., 2011/43, Lower Hutt, New Zealand, 121 pp., 2011.

Wang, X., Lukovic, B., Power, W. L., and Mueller, C.: High-resolution inundation modelling with explicit buildings: a case study of Wellington CBD, GNS Sci. Rep., 2017/13, 27 pp., 2017.

Wang, X., Holden, C., Power, W., Liu, Y., and Mountjoy, J.: Seiche effects in Lake Tekapo, New Zealand, in an Mw 8.2 Alpine Fault earthquake, Pure Appl. Geophys., 177, 5927–5942, doi:10.1007/s00024-020-02595-w, 2020